Materials Characterization 159 (2020) 110014

Contents lists available at ScienceDirect

Materials Characterization

journal homepage: www.elsevier.com/locate/matchar

Habit planes of twins in a deformed Mg alloy determined from three-dimensional microstructure analysis

Farangis Ram[a,1], Jeffrey T. Lloyd[b], Gregory S. Rohrer[a,*]

[a] Department of Materials Science and Engineering, Carnegie Mellon University, Pittsburgh, PA 15213, USA
[b] US Army Research Laboratory, Aberdeen Proving Ground, MD 21005-5066, USA

ARTICLE INFO

Keywords:
3D EBSD
Mg alloy
Twins
Boundary distributions

ABSTRACT

Serial sectioning and electron backscatter diffraction were used to image the three-dimensional microstructures of Mg alloy AZ31B deformed in tension and compression along sample directions that promote twinning. These measurements were used to statistically determine the habit planes of twin boundaries within the samples. For the sample deformed in tension, the boundary population is dominated by the so-called extension twin (lattice disorientation of 86° about $[2\bar{1}\bar{1}0]$ with symmetric $(01\bar{1}2)$ boundary planes) and boundaries formed by the intersection of these defects (lattice disorientation of 60° about $[01\bar{1}0]$ with $\{11\bar{2}1\}$ and $\{01\bar{1}1\}$ boundary planes). The sample deformed in compression, however, was different. Fewer twin variants were activated and this led to many fewer intersections and intervariant boundaries. Furthermore, while the dominant boundary also had the lattice disorientation of 86° about $[2\bar{1}\bar{1}0]$, consistent with an extension twin, the dominant habit planes have the asymmetric $(0\bar{1}11)$ and $(01\bar{1}3)$ orientations. The difference in the habit planes was attributed to the presence or absence of twin intersections. When many twins intersect, the twins form plate-shaped grains, bounded by two parallel $(01\bar{1}2)$ interfaces. Without these intersections, the twins are wedge-shaped, with the bounding $(0\bar{1}11)$ and $(01\bar{1}3)$ interfaces meeting at a sharp edge.

1. Introduction

Twinning plays an important role in both the plastic deformation and ultimate mechanical failure of Mg and its alloys [1–7]. The primary twins in Mg form on pyramidal planes, with the $\{10\bar{1}1\}$, $\{10\bar{1}2\}$, and $\{10\bar{1}3\}$ planes being the most commonly cited. When twinning occurs on the $(10\bar{1}1)$ plane, the shear is in the $[10\bar{1}\bar{2}]$ direction. This deformation leads to a contraction along the c-axis and it is therefore referred to as the contraction twin. When twinning occurs on the $(10\bar{1}2)$ plane, the shear is in the $[\bar{1}011]$ direction [8]. Because this deformation leads to an extension along the c-axis, it is referred to as an extension twin. According to Koike [9], the $\{10\bar{1}2\}$ twin is active at a small fraction of the stress needed to activate the $\{10\bar{1}1\}$ twin. The $\{10\bar{1}2\}$ extension twin is also found in samples that have been compressed. Compression perpendicular to the c-axis elongates the crystal along the c-axis and this deformation is accommodated by extension twins. Compression along the c-axis may also activate extension twins in response to anomalous stress states created by the deformation of neighboring grains [10]. Note that throughout this manuscript, the designation “twin” will refer to a deformation twin rather than an annealing twin.

Other twin related boundaries arise from double twinning or from boundaries between twin variants. Double twinning results when a crystal twins first on one of the pyramidal planes, say $\{10\bar{1}1\}$ or $\{10\bar{1}3\}$, and then twins again on a $\{10\bar{1}2\}$ plane. The material formed by the second twin has a new orientation relationship with the parent grain. Boundaries between twin variants form when separate twins, on different $\{10\bar{1}2\}$ variants, form within the same parent grain. If the variants grow and meet to form a new interface, an intervariant boundary is formed. For example, when twins on $(10\bar{1}2)$ and $(01\bar{1}2)$ planes within a single grain meet, a new boundary with a 60° rotation about an axis that is 3.7° from $\langle 10\bar{1}0\rangle$ is formed [10,11]. The statistics of twin distributions in deformed Mg have been reported previously [10–13]. Interestingly, it has recently been pointed out by Sun et al. [14] that the number of allowed twinning modes greatly exceeds the number of modes that have been reported in the literature. These authors speculated that the focus of research on the well-known twin types may be a result of selection bias. In the present work, we analyze all twins within the measured volume to identify the habit planes.

The classical method for designating different twinning modes was originally described by Bilby and Crocker [15–17]. An alternate method

* Corresponding author.
E-mail addresses: fram@evrazna.com (F. Ram), jeffrey.t.lloyd.civ@mail.mil (J.T. Lloyd), rohrer@cmu.edu (G.S. Rohrer).
[1] Current affiliation: EVRAZ NA, 14400 N Rivergate Blvd, Portland, OR 97229, USA.

https://doi.org/10.1016/j.matchar.2019.110014
Received 22 July 2019; Received in revised form 24 October 2019; Accepted 12 November 2019
Available online 14 November 2019
1044-5803/

of describing the twins (and any other boundaries) in Mg is to specify five parameters describing the boundary geometry. Usually, three parameters describe the lattice disorientation and two parameters describe the boundary plane orientation [18]. For example, the common $\{10\bar{1}2\}$ extension twin in Mg can be described as an 86° rotation around the $[1\bar{2}10]$ axis, with a $(10\bar{1}2)$ grain boundary plane and is written as $86°/[1\bar{2}10]|(10\bar{1}2)$. Note that the crystallographic orientation of the second grain boundary plane is fixed by these parameters; in this particular case the boundary plane orientation is the same in both crystals, meaning that it is a symmetric boundary. This method for describing boundaries has the advantage of being directly related to observable quantities that result from modern electron backscatter diffraction experiments, and in general we will adopt this description throughout this paper. While the Bilby-Crocker [15] method has the advantage that the description includes the shear component of the deformation, the shear component of a twin cannot be evaluated by diffraction alone.

The three dimensional shapes of twins in Mg have not been investigated in detail. In the vast majority of studies, the twins have been imaged in plane sections [3,4,10–13,19,20] or electron transparent thin foils [5,21–24]. In such cases, it is typical that the lattice misorientation is used to assign the twin mode. Even when the orientation of the boundary's intersection with the section plane is measured, considerable uncertainty remains because the orientation of the boundary about that line of intersection is unknown (it may be anywhere within the zone of the line). To be certain of the orientation of a boundary within a microstructure, it is necessary to have orientation data in all three spatial dimensions. To date, there are only two studies that have reported 3D data for the structure of twins in Mg [25,26]. Neither of these studies reported on the distribution of interface planes or identified the habit planes of the twins.

The purpose of this paper is to report the three-dimensional structure of twins in Mg alloy AZ31B derived from a statistical analysis of the crystallographic orientations of the twin boundary habit planes. The work uses three-dimensional electron backscatter diffraction (3D-EBSD), which has become feasible with the implementation of dual-beam FIB-SEMs. These instruments are scanning electron microscopes (SEMs) equipped with a focused ion beam (FIB). The FIB-SEM makes it possible to record planar orientation maps on serial sections of the sample [27,28]. From a 3D-EBSD measurement, it is possible to determine both the lattice misorientation across the boundary and the orientations of the boundary planes. The orientation of the boundary plane is important because it influences both the properties of the boundary [29] and the macroscopic properties of the polycrystal [30]. Two low strain deformed samples are compared: one strained in tension and one strained in compression. The dominant planar defect in both samples is the extension twin with a $86°/[1\bar{2}10]$ misorientation. The measurements show that the interface planes in the tension and compression samples are not the same and this is likely because of the many twin intersections in the tension sample and the lack of such intersections in the compression sample.

2. Experimental

Magnesium AZ31B plates, 2″ thick, were received in the H24 condition from Magnesium Elektron. The plates measured approximately 12″ × 12″ in the rolling and transverse directions. The plates were subsequently annealed at 350 °C for 1 h to remove effects of prior straining. X-Ray diffraction measurements indicate that the material displayed conventional magnesium rolling texture where the basal planes are preferentially aligned with the plate normal direction. The specimens were extracted from a rolled plate; one was strained to 6% elongation in the plate normal direction and other was strained to 6% compression in the plate rolling direction, similar to previous work that studied effects of loading on twin morphology evolution [6].

The 3D-EBSD measurements were accomplished by serial sectioning using a FEI Helios™ PFIB DualBeam™ equipped with an Oxford Instruments NordlysMax^3 EBSD camera. Each measured volume was a part of an approximately 10 mm × 5 mm × 5 mm sample. In each sample, the surface that was parallel to the measured slices was prepared by mechanical polishing down to 0.05 μm colloidal silica prior to mounting the sample to the microscope. Before collecting the 3D EBSD data, the specimens were cleaned by removing about 2 μm from all their surfaces using the PFIB. The serial sectioning was accomplished with a 30 kV, 59 nA Xe plasma beam. For collecting the EBSD maps, the SEM was operated with a 20 kV, 9 nA electron beam. The binning on the EBSD camera chip was set to 4 × 4 and the acquisition speed was about 4 Hz. The indexing rate remained above 90% and the mean MAD (mean angular deviation, a parameter used by the Aztec software to quantify the reliability of the measured crystal orientation) was 0.6°. A lower MAD means a higher confidence in the determined crystal orientation.

For the sample that had been loaded in tension, 116 parallel layers, each 100 μm by 50 μm and separated by 0.4 μm, were recorded. Within each plane, orientations were recorded every 0.4 μm on a square grid so that the size of a cube shaped voxel is 0.4 μm × 0.4 μm × 0.4 μm. The total measured volume is 100 μm × 50 μm × 46.4 μm = 232,000 μm^3. For the sample that had been loaded in compression, 198 parallel layers, each 125.2 μm by 27.2 μm and separated by 0.4 μm, were recorded. Using the same grid as for the tension sample, the data is also comprised of 0.4 μm × 0.4 μm × 0.4 μm cube shaped voxels. The total measured volume is 125.2 μm × 27.2 μm × 79.2 μm = 270,000 μm^3.

The stack of two-dimensional parallel layers was reconstructed into a 3D volume using DREAM.3D [31]. The sequence of steps used (referred to as a pipeline) was similar to the software's default pipeline available for reconstruction, clean-up, and the calculation of the grain boundary distributions. First, the two-dimensional orientation maps were aligned by maximizing the overlap of pixels of similar orientations, belonging to adjacent layers and differing by no > 5°. The orientation data were cleaned by iteratively assigning each voxel with undetermined orientations to the orientation of the most reliable neighbor. Clusters of 16 or more voxels with orientations that differ by no > 5° were segmented into grains and all voxels within each grain were assigned the average orientation. The choice of a minimum grain size of 16 voxels is found to balance the desire for high spatial resolution with the ability of the grain boundary meshing algorithm to produced smoothly curved grain boundaries. A minimum disorientation of 5° was selected because, based on the disorientation distribution, very few real boundaries are expected to have disorientations < 5° yet this threshold still eliminates artificial boundaries that might arise from uncertainty in the orientation measurement. The cropped, cleaned-up volumes are illustrated in Fig. 1, where the grains are colored by their orientation with respect to the milling direction.

A triangular mesh was created to represent the internal boundaries and then smoothed to remove the stepped structure associated with the voxels. For the sample deformed in tension, there were > 1.5 × 10^6 triangles in the mesh and for the sample deformed in compression there were > 7.7 × 10^5 triangles. For each triangle, the orientation of the normal in the sample reference frame is known, the area is known, and the orientations of the crystals on either side are known. From these data, it is possible to compute the distribution of the boundary area over the five crystallographic parameters [18]. To determine the distribution of boundary planes at fixed misorientations we used the kernel density method [32], with a 5° limit for misorientations and a 7° limit for the grain boundary plane orientations. For the disorientation distributions and axis-angle distributions, the domain of parameters is discretized and each triangle is classified into a discrete bin to determine the distribution [33–35].

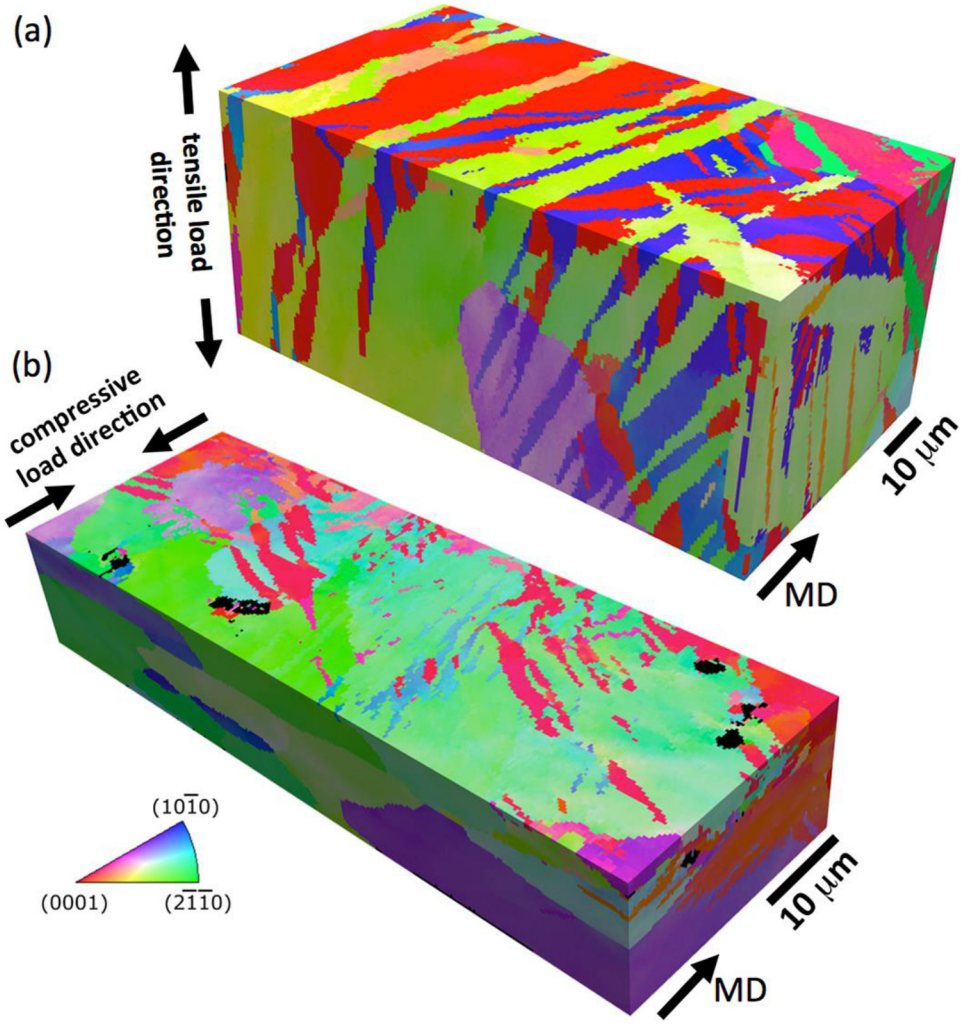

Fig. 1. Reconstructed volumes of the sample deformed in (a) tension and (b) compression. MD denotes the milling direction. In (a), the tensile load direction is the plate normal direction and the rolling direction is along the milling direction. In (b), the rolling direction is along the compressive load direction and the normal direction is vertical.

3. Results

3.1. Interface distributions

The distribution of disorientation angles (minimum misorientation angles) for the sample deformed in (a) tension and (b) compression are illustrated in Fig. 2. The distributions were calculated from all of the boundary triangles and discretized with a resolution of 1°. The red dashed line represents the distribution that would be expected if the boundaries were distributed randomly over the three disorientation parameters. Note also the break in the vertical axis. For the sample that was deformed in tension (a), the distribution significantly exceeds random in the range between 56° and 60° and between 83° and 90°. In fact, 80% of all the boundary area is within these two angular ranges. For the sample deformed in compression, the distribution also significantly exceeds random in the range between 83° and 90°; 51% of all boundary area is within this disorientation range. There are smaller maxima in the range between 10° and 35°, but these are the result of general boundaries, which can be seen in Fig. 3b. The absence of a peak in the vicinity of 60° for the compression sample is significant. As discussed later, this disorientation arises from twin intersections and the absence of a maximum at this disorientation indicates that twin intersections are less common in the compression sample.

Fig. 3 shows the interfaces within the two samples, colored by disorientation angle. The limited number of colors, and their associated disorientations, are consistent with the distributions in Fig. 2. For example, in the image in Fig. 3a, of the sample deformed in tension, many of the boundaries are colored from orange to red, representing boundaries with disorientations between 83° and 90°, or a grey to beige color, representing boundaries with disorientations between 45° and 60°. In the image in Fig. 3b, of the sample deformed in compression, many of the boundaries are colored from orange to red, representing boundaries with disorientations between 83° and 90°, or a shade of blue, corresponding to general boundaries with disorientations between 10° and 35°. The limited range of disorientation angles for the general grain boundaries results from the [0001] texture; the domain of unique rotations about [0001] is 0 to 30°. The blue colored boundaries create the peaks at low angles in the disorientation angle distribution shown in Fig. 2b. To provide a sense of scale, note that Fig. 3a & b are the same two volumes displayed in Fig. 1a and b, in approximately the same orientation.

To learn more about the crystallographic character of the most common boundaries in these samples, we can inspect the distribution of misorientation axes at the disorientation angles where is distribution maximizes. To determine the disorientation axis distributions, the boundaries were classified in discrete bins with a width of 7.5° in all three Euler angles. For the sample deformed in tension, the distributions centered at 57° and 90° are shown in Fig. 4a and b, respectively.

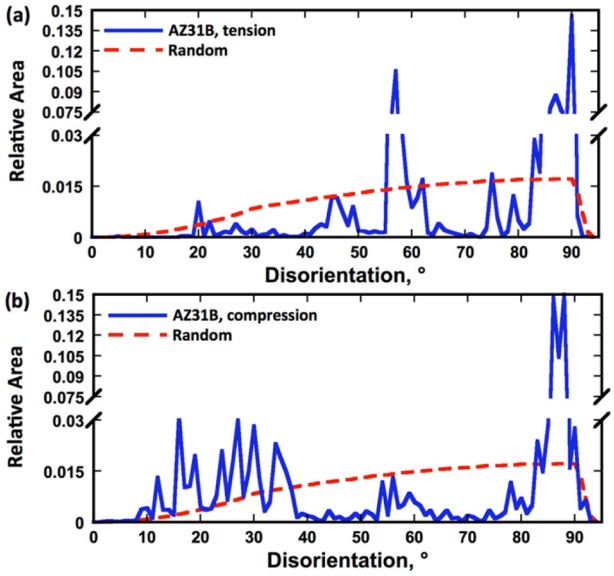

Fig. 2. Disorientation angle distributions in AZ31B for the sample deformed in (a) tension and (b) compression. The dashed line shows the distribution expected for a random distribution of boundaries. The random distribution was computed from 5×10^6 randomly generated pairs of crystal orientations.

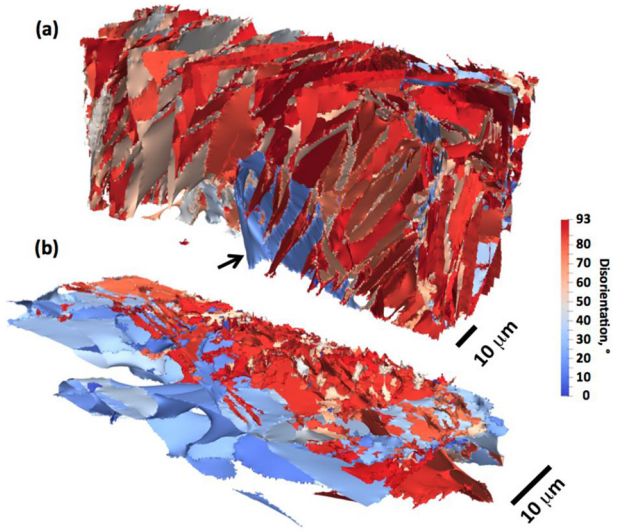

Fig. 3. Images of the interfaces in the two samples, colored by disorientation. (a) The sample deformed in tension. The arrow is provided as a reference for the description of Fig. 10. (b) The sample deformed in compression.

We select 57° and 90° because these are the maxima in the disorientation distributions in the tensile sample. Note that the 'ideal' twin misorientations of 86.3° for the extension twin and 60° for the intervariant boundary between the $(10\bar{1}2)$ and $(01\bar{1}2)$ variants are, at this level of discretization, equivalent to 57° and 90°. When the axis-angle distributions are plotted at the 'ideal' angles, they have the same shape with a smaller intensity. One reason for the spread in the range of angles is the deformation of the sample. The deformation creates some lattice curvature (note the different shades of color within the grains in Fig. 1) so that any disorientation between two grains is not likely to be the ideal value. For the sample deformed in compression, the axis distribution at 90° is shown in Fig. 4c. For a disorientation of 90° in both the tension and compression samples, the maximum is reached at the $[2\bar{1}\bar{1}0]$ direction. For the 57° disorientation in the sample deformed in tension, there is a maximum very near the $[10\bar{1}0]$ axis; it is actually rotated by about 4° from the ideal orientation. Therefore, the interfaces that make up the majority of the grain boundary area in the tension sample are 90°/$[2\bar{1}\bar{1}0]$ and 57°/$[10\bar{1}0]$. For the sample deformed in compression, it is 90°/$[2\bar{1}\bar{1}0]$.

The difference in the frequency of twin boundaries between the two samples can be understood in terms of the Schmid factor analysis on twin systems due to the loading direction with respect to the sample orientation [6]. For the sample compressed along the normal direction, assuming the $[2\bar{1}\bar{1}0]$ direction is evenly distributed, only one twin variant pair has a Schmid factor approaching 0.5. Within a grain a single dominant twin is expected to grow and relax the stress on other twin systems before they can activate, thus preventing 57°/$[10\bar{1}0]$ twin-twin boundaries from forming. However, when the sample is pulled in tension along the plate normal, six twin variants are highly stressed with Schmid factors approaching 0.5. Deformation within grains is expected to occur by multiple twins nucleating simultaneously and interacting to form a large number of intervariant 57°/$[10\bar{1}0]$ boundaries. The twin morphology for these two cases has been observed elsewhere [6], and is consistent with the simple Schmid factor analysis.

The boundary plane distributions at the three disorientations indicated by the maxima in Fig. 4 are illustrated in Fig. 5. The distributions are plotted on stereographic projections using the method described by Glowinski [32]. Recall that the smoothly curved interfaces visualized in Fig. 3 are made up of many individual triangles; each of them is treated independently when computing the distributions in Figs. 2, 4, and 5. The 90°/$[2\bar{1}\bar{1}0]$ boundary in the sample deformed in tension is a symmetric boundary with the same plane $(01\bar{1}2)$, on both sides of the boundary. Note that the distribution at the 'ideal' misorientation, 86°/$[2\bar{1}\bar{1}0]$, has the same maxima, but the intensities are not equal. The two peaks are equal in the distribution of boundary orientations at 90° because the kernel overlaps with equal numbers of boundaries at the ideal 86.3° rotation and the indistinguishable 93.7° rotation. When the kernel is moved away from the symmetric position, it favors one representation and the peaks are unequal. For the 57°/$[10\bar{1}0]$ boundary, there are two main boundary types (here, the misorientation axis has been rotated by 4° from $[10\bar{1}0]$ to the maximum of the axis-angle distribution). The first is a twist boundary on $\{1\bar{2}11\}$ planes and the other is an asymmetric boundary whose nearest low index planes are $(01\bar{1}1)$ and $(\bar{1}\bar{1}2\bar{1})$. The 90°/$[2\bar{1}\bar{1}0]$ boundary in the sample deformed by compression is distinct from the one in the sample

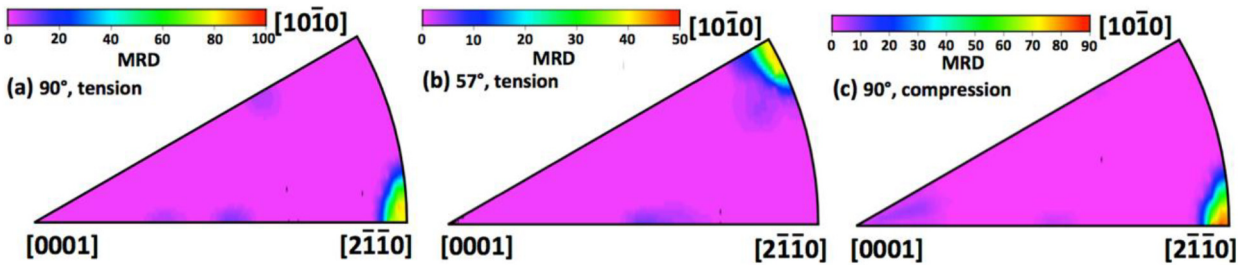

Fig. 4. The distribution of disorientation axes at (a) 90° and (b) 57° for the sample deformed in tension and (c) 90° for the sample deformed in compression. The distributions are plotted in the standard stereographic triangle for hexagonal crystals. The units, MRD, are multiples of a random distribution.

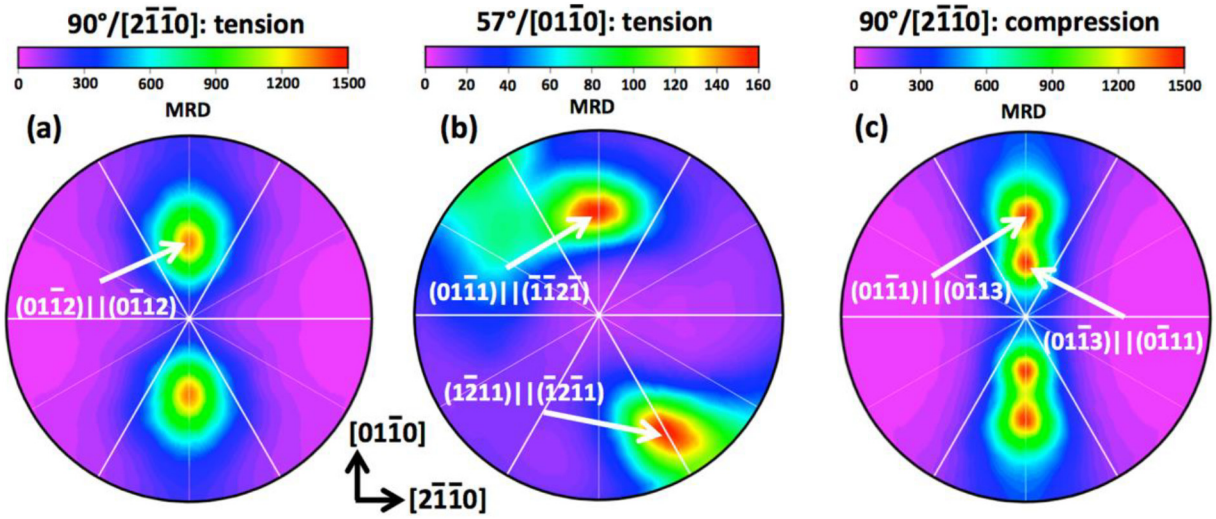

Fig. 5. Boundary plane distributions at fixed misorientations. The distributions are plotted in stereographic projection. (a) 90°/[2$\bar{1}\bar{1}$0] in the tension sample. (b) 57°/[10$\bar{1}$0] in the tension sample. (c) 90°/[2$\bar{1}\bar{1}$0] in the compression sample.

deformed by tension. Instead of symmetric (01$\bar{1}$2) planes, there is a distribution of asymmetric tilt boundaries with maxima at the (01$\bar{1}$1)||(0$\bar{1}$13) configuration. Note that the distribution at the 'ideal' misorientation, 86°/[2$\bar{1}\bar{1}$0], has the same maxima, but the intensities are not equal. Because the interfaces are not completely flat and the meshing of a discrete voxelized microstructure always has some uncertainty, there is high intensity along much of the [2$\bar{1}\bar{1}$0] zone and, at the symmetric (01$\bar{1}$2) orientation, the intensity is approximately 80% of the nearby maxima at the (01$\bar{1}$1)||(0$\bar{1}$13) configuration.

To clearly show the difference in the distribution of habit planes for the two samples, Fig. 6 shows the relative grain boundary area along the zone of tilt boundaries for the 90°/[2$\bar{1}\bar{1}$0] boundary in the tension and compression samples. For these plots, the distribution is sampled every 3°. For the tension sample, the maximum is less than the sampling interval (3°) from the ideal (01$\bar{1}$2) orientation. The maxima in the distribution for the compression sample are also within 3° of the ideal (01$\bar{1}$1) and (0$\bar{1}$13) orientations. What this means is that the twins in the two samples have different shapes and very different interface structures.

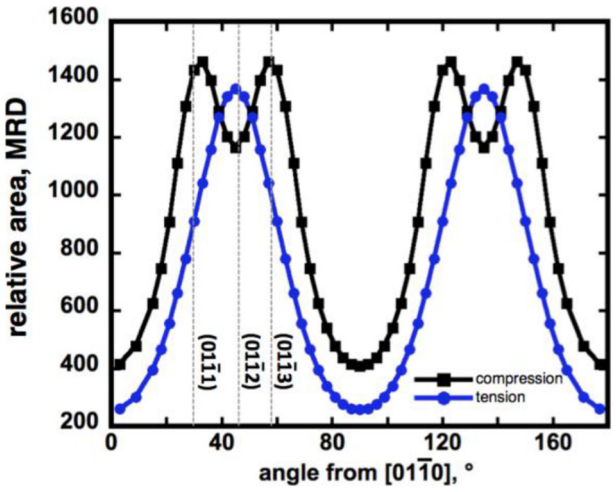

Fig. 6. Relative areas of boundary planes along the tilt axis of the 90°/[2$\bar{1}\bar{1}$0] boundary in the tension (circles) and compression (squares) samples. The maxima in the boundary plane distributions occur at distinct orientations.

3.2. Twin shapes

The shapes of the twins in the tension sample should be, on average, similar to a parallelepiped, so that it can be bounded by two parallel (01$\bar{1}$2) oriented boundaries. On the other hand, the twins in the compression sample should be, on average, wedge shaped with two non-parallel boundaries with the (01$\bar{1}$1) and (0$\bar{1}$13) orientations. Such shapes are easily found in the sample. For example, Fig. 7 shows two neighboring twins. The misorientation coloring in (a) is used to show the large faces have approximately 90° disorientations. The lateral boundaries are intervariant boundaries in the 45° to 60° range formed by the intersection with another twin. In (b), the same grains are colored by the interface orientation, with the dominant color corresponding to the (01$\bar{1}$2) orientation. This orientation is indicated on the legend by the arrow. The opposite sides of the same grains are shown at reduced scale in (c) to verify that the boundary orientations are similar.

The twins in the compression sample are different, as illustrated in Fig. 8. The image in Fig. 8a, colored by disorientation, shows a large twin interface with three knife-edged protrusions labeled by arrows. The interface has the characteristic disorientation of the twin. When the exact same region is colored interface orientation (see Fig. 8b), it is clear that the top and bottom surfaces of the knife-edge have different orientations. The top surface is oriented in the vicinity of (0$\bar{1}$13) and the bottom interface is oriented near (01$\bar{1}$1). These orientations are indicated on the legend by the two arrows. Note that the two interfaces form a wedge shape with two different interface orientations. These shapes are characteristic of the twins that are not intersecting other twins. This might be the origin of the different twin shapes in the tension and compression sample, a point we will elaborate on in the discussion section.

In addition to making it possible to identify the habit planes, the three-dimensional data also makes it possible to understand how the different twin boundaries interact. An example is illustrated in Fig. 9. A small portion of the outer surface of the sample deformed in tension is shown in Fig. 9a and selected interfaces between some of these grains, colored by disorientation, are shown in Fig. 9b. Numerical labels from 1 to 7 are found in 9a and 9b to denote the same regions. This region is made up of crystals with four orientations: red (1 & 3), green (5 & 7), blue (4 &6), and orange (2). Because of the interpenetration of the twins, it is difficult to label one as the parent. However, we can see that the boundaries 4/3, 3/6, 5/2, and 2/7 are all colored to indicate they have a disorientation between 83° and 90° (the notation N/M denotes the boundary between grain N and M). Meanwhile the 2/3, 2/1, 5/1,

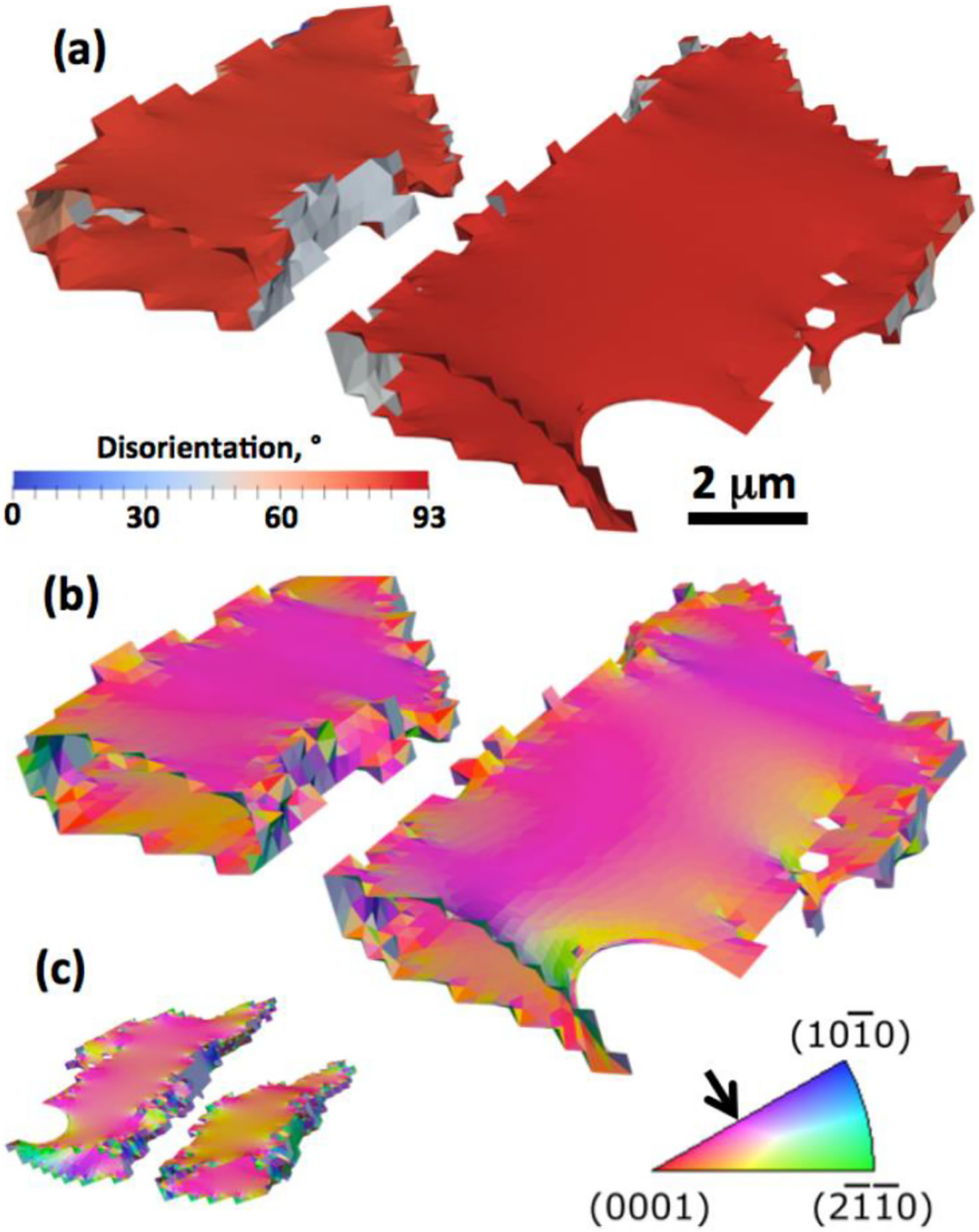

Fig. 7. Two parallel twins in the tension sample. (a) Interfaces colored by disorientation. (b) Colored by orientation. (c) Opposite side, colored by orientation, at reduced scale.

and 7/1 boundaries are colored with disorientations in the 45° to 60° range. So, the two main types of boundaries are those between twins and those between different twin variants. These two types of interfaces make up the two types of boundaries discussed above.

It is also possible to find examples of twins apparently passing through general grain boundaries. Some twins that are continuous across a boundary in the sample deformed in tension are illustrated in Fig. 10. The blue interface in Fig. 10a is a general grain boundary and the red interfaces are twins. The twins are continuous in the grain below the blue general boundary. While the twins in that lower are, for clarity, not shown in Fig. 10a, they can be seen in Fig. 3a, were the position of the same general grain boundary is indicated by the black arrow. On the general grain boundary in Fig. 10a, there are beige colored areas, such as the one indicated by the white arrow. These are boundaries with the twin in the lower grain, where it has not penetrated the upper grain. In most cases, the twin in the lower grain is larger than in the upper grain, suggesting that the general boundary provides a resistance for the penetration of the twin [12,36]. The shapes at the leading edges of the twins are also interesting. The twin in Fig. 10a denoted by the black arrow is shown in profile, colored by the interface

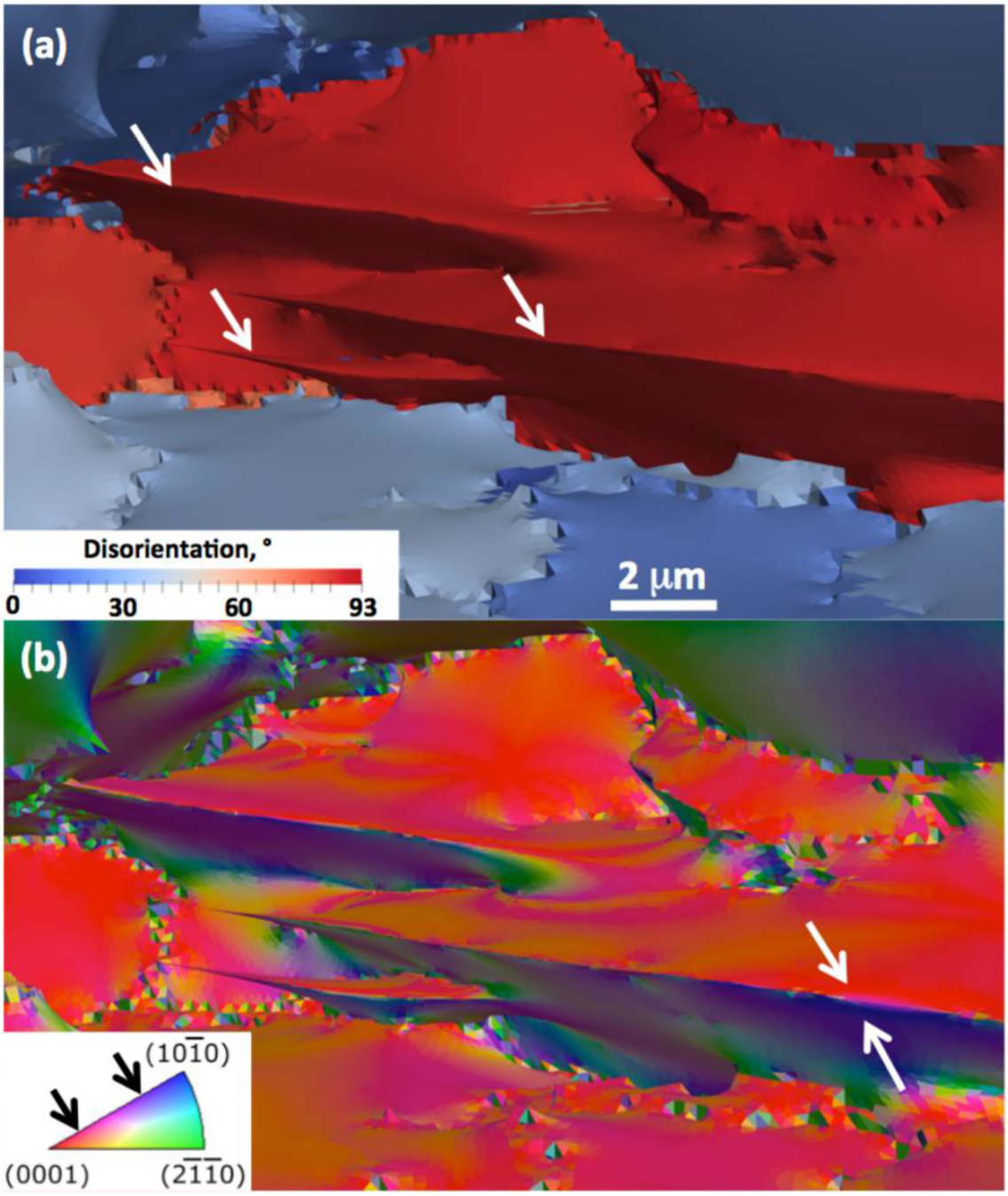

Fig. 8. The shape of a twin interface in compression sample. (a) Interfaces colored by disorientation. (b) Interfaces colored by orientation.

orientation, in Fig. 10b. Note the semi-circular shape of the interface at the edge of the twin. This same shape can be found at the edge of one of the twins in Fig. 7 and is a common observation at the leading edges of the twins. While the origin of the semi-circular shape is not known, it is possible that the twin is advancing around a defect or precipitate where there is a resistance to the shear associated with twinning.

4. Discussion

For the sample deformed in tension, two boundary types dominate the population. The first is the well-known extension twin, a boundary with parameters that are ideally 86°/[1$\bar{2}$10]|(10$\bar{1}$2). For the sample deformed in tension, there is also a high population of boundaries with disorientations in the range of 56° to 60°. While this angular range is reasonably close to the expected disorientations for the {10$\bar{1}$1} and {10$\bar{1}$3} compression twins at 56° and 64°, respectively, the axis of disorientation, [10$\bar{1}$0], is not consistent with this twinning mode. Instead, this population of boundaries arises from the intersections of different twin variants. This is verified by Fig. 9. It is interesting to note that the boundary planes separating twin variants are non-random, favoring low index planes.

Yu et al. [23] referred to the intersection of two twins as twin-twin boundaries (TTB). Using their terminology, they defined the type I TTBs as forming between twins that share a < 11$\bar{2}$0 > zone axis. They concluded that type I TTBs should be low disorientation angle tilt boundaries with a basal or prismatic orientation. They also defined type II TTBs as having a different zone axis and a high index crystallographic plane orientation that might relax to a lower energy orientation. Based

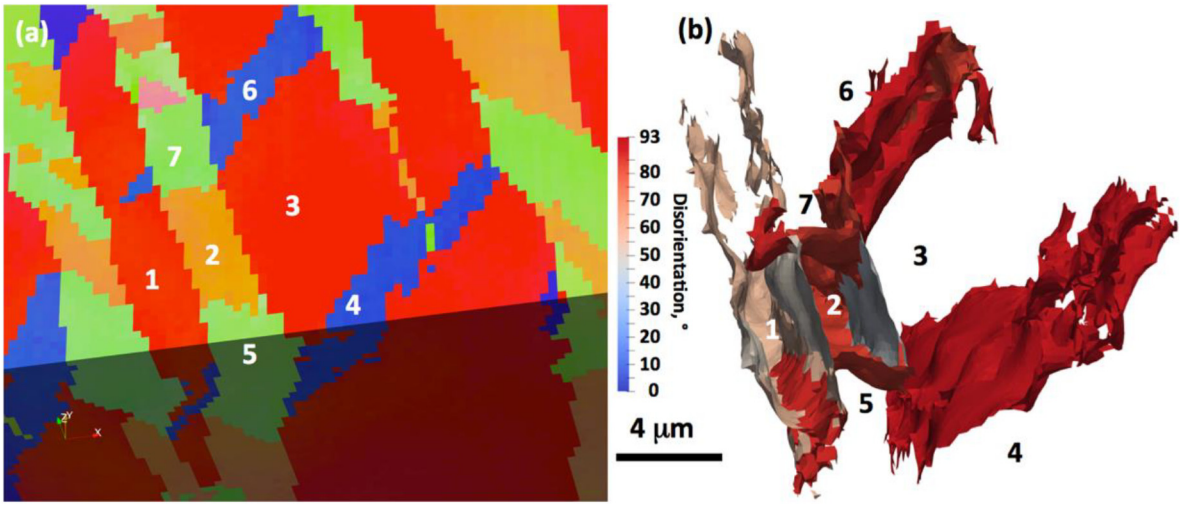

Fig. 9. Detail of the grain orientations (a) and the interface disorientations (b) in a small region of the sample deformed in tension. The orientation colors are the same used in Fig. 1. The numerical labels identify the same orientation regions in (a) and (b).

on these definitions, and the observed boundary character, we find only type II TTBs. The low indices of the boundary orientations, and the prevalence of the $(1\bar{2}11)$ twist boundaries, suggest that they have relaxed away from the high index orientations predicted from the earlier two-dimensional observations [23].

When discussing the boundary plane orientations, it is important to note that they are not strictly planar. This is clear in the images (for example, Fig. 1) because the twin boundaries do not intersect the surface in straight parallel lines. Some of the non-planarity certainly results from the discretization of the measurement, but a large component is simply the non-ideal shape of the twins. Thus, when we say the symmetric twins in the tension sample are $86^\circ/[1\bar{2}10]|(10\bar{1}2)$, it means the distribution of grain boundary planes reaches a maximum at this orientation (see Fig. 6), but there is a range of observed orientations about the symmetric orientation. The same can be said about the distribution of asymmetric tilt boundaries found in the compression sample. Compared with the tension sample, there is an even broader range of orientations permitted in the $[2\bar{1}\bar{1}0]$ zone. The separation between the $(0\bar{1}11)$ and $(0\bar{1}13)$ orientations is 30° and the breadth of the distribution of possible boundary planes observed in the compression sample extends beyond this 30° range.

It is worth considering the possibility that the source of the difference in the interface plane distribution for the $86^\circ/[2\bar{1}\bar{1}0]$ boundary in the tension and compression samples is created by the data processing rather than characteristics of the samples. The $(0\bar{1}11)$ with $(01\bar{1}3)$ planes are separated by 30° and this is much larger than the resolution of the techniques. The boundary distributions are computed with resolutions of 5° in misorientation space and 7° in the boundary orientation space, both significantly smaller than 30°. The distributions were computed at higher resolution (3° for misorientation and 5° for boundary orientation) and this led to stronger maxima at the $(0\bar{1}11)$ with $(01\bar{1}3)$ positions and a deeper local minimum at the $(0\bar{1}12)$ position. A second factor that plays a role is the reconstruction of the microstructures in three-dimensions is the meshing used to construct the interfaces. However, the voxel size of the data is exactly the same and identical procedures and parameters were used for the reconstruction and meshing of the microstructures. Therefore, the difference in the boundary plane orientations is not the result of data processing. Furthermore, if one carefully looks at the shapes of the boundaries with the 86° misorientations in Fig. 3b and d (the red ones), they appear similar to one another with respect to their smoothness and curvature. Finally, the boundary plane distributions were also calculated using a separate set of codes (outside

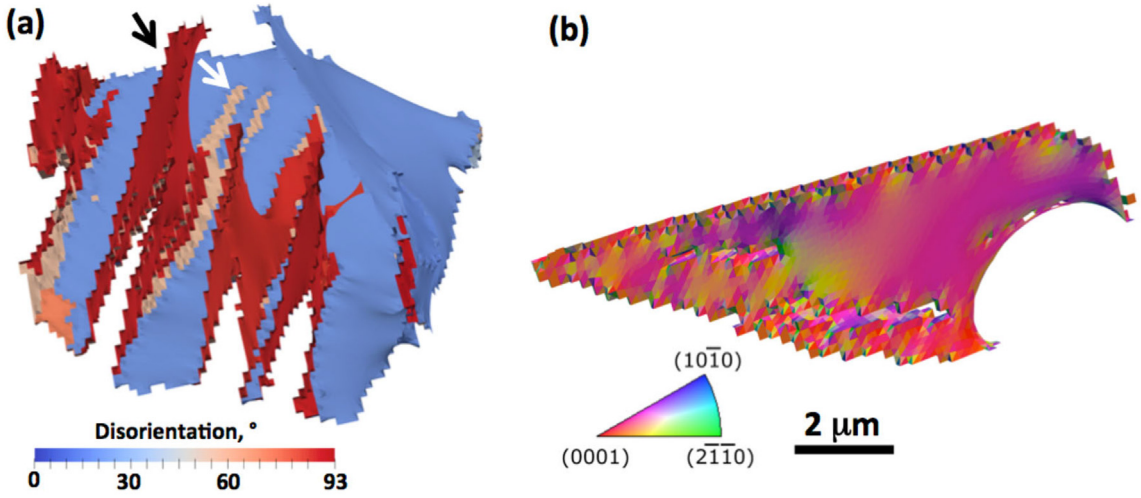

Fig. 10. (a) Twins (red) emerging from a general boundary (blue) as a continuation of twins in the neighboring grain (not shown). Interfaces are colored by disorientation. (b) A view of the twin denoted by the black arrow in (a), colored by interface orientation. (For interpretation of the references to color in this figure legend, the reader is referred to the web version of this article.)

Dream.3D) that classify the boundary planes in discrete bins and have been described previously [33–35]. These codes yielded the same results. Based on this, we conclude the differences in the boundary plane orientations are a characteristic of the samples, not the analysis methods.

The observation of asymmetric boundary planes has received some attention in the past, but these reports were based on two-dimensional observations and no attempts were made to measure the distribution [21,22,24,37,38]. For example, in transmission electron microscopy studies of 86°/[$1\bar{2}10$] twins, significant deviations from the ideal boundary plane have been reported [21,22]. Similarly, Ostapovets et al. [38] showed, based on two-dimensional line traces of twins in Co, that much of the boundary trace was not consistent with {$10\bar{1}2$} boundary planes and Liu et al. [37] and Wu et al. [24] both reported on "twin-like" boundaries with the 86°/[$1\bar{2}10$] disorientation, but without a mirror plane. Deviations from the ideal plane can be accommodated microscopically by so-called "basal||prismatic" (BP) facets; these are sections of the interface where the (0001) and ($10\bar{1}0$) planes are parallel. Note that the (0001) and ($10\bar{1}0$) planes are not exactly parallel at the 86° misorientation, so the lattice has to be strained to make them parallel. Hence, the so-called BP facet is a defect that involves strain. Paidar et al. [39,40] have shown that BP facets are relatively low energy boundary defects that alter the orientation of the interface. Such segments are especially important for the growth of the twin [38,41]. However, BP facets can also result from plastic deformation. It has been shown by simulation that BP facets can form when dislocations intersect the twin boundary [42–44]. If dislocations are gliding on the basal plane in a grain with twins, they will eventually intersect the {$10\bar{1}2$} twin boundary. Each time this happens, a BP facet is incorporated into the interface and the interface orientation changes. The BP facets in twin boundaries are nm-scale features; El Kadiri et al. [44] report that the most stable length of the BP facet is roughly 10 times the interatomic spacing. Therefore, if these defects accommodate the deviations from the ideal ($10\bar{1}2$) orientation, we would not resolve them as individual defects, but as an asymmetric boundary orientation.

The observed difference in the habit planes of the twins in the two samples appears to be related to the proliferation of intersecting twins in the sample deformed in tension. This creates roughly planar intervariant boundaries at the ends of the plate-shaped twin that make it possible for the larger facets of the plate to be parallel and close to the ideal ($10\bar{1}2$) orientation (as in Fig. 7). In the sample deformed in compression, however, there is one dominant twin variant and, therefore, few intersections. In fact, the intervariant boundaries have a relative area smaller than expected in a random distribution (see Fig. 2b). Because of this, these twins tend to be wedge shaped, with two non-parallel lateral surfaces, as illustrated in Fig. 8. Instead of random high index planes, the habit planes are low index pyramidal planes with the ($0\bar{1}11$) with ($01\bar{1}3$) orientations. Far from the leading edge, the interfaces may be closer to the ($10\bar{1}2$) orientation, but when all the interfaces within the sample are considered, it is the asymmetric ($0\bar{1}11$) with ($01\bar{1}3$) orientations that dominate the crystal habit of the twins in the sample deformed in compression.

In summary, we think there are two factors that contribute to the differences in the twin habit planes in the compression and tension samples. The first is that in compression, fewer twin variants are activated and as a result there are fewer intersections. This allows the twins in the compression sample to adopt wedge shapes; these non-parallel lateral boundary planes cannot have the symmetric {$01\bar{1}2$} orientation. On the other hand, when there are many intersecting twins, as in the tension sample, and the twins are bound on some sides by intervariant boundaries, they form shapes more like parallelepipeds which permit parallel symmetric boundaries on the lateral sides. A second contributing factor to the difference in shape of the twins formed in compression and tension is the interaction of the twins with basal dislocations. Because fewer twin variants are activated in compression, there must be additional dislocation activity to accommodate the strain. When basal dislocations intersect twins, they create interface defects that reorient the boundary to an asymmetric configuration [42–44]. The extent to which these two proposed mechanism contribute to the asymmetric twin boundary formation will be the subject of future research.

5. Conclusion

The microstructures of Mg alloy AZ31B that have been loaded in compression and in tension have been compared. The dominant planar defect introduced by the deformation of both specimens is a boundary with an 86° rotation about [$2\bar{1}\bar{1}0$]. For the sample deformed in tension, this is the well-known extension twin with symmetric {$01\bar{1}2$} interface planes. Intervariant boundaries between these twins tend to terminate on low index pyramidal {$\bar{1}2\bar{1}1$} and {$01\bar{1}1$} planes. However, for the sample deformed in compression, fewer variants are created. In this case, the dominant habit planes for the interface with an 86° rotation about [$2\bar{1}\bar{1}0$] are ($0\bar{1}11$) with ($01\bar{1}3$), which form the faces on wedge shaped twins. The difference between the habit planes of the twins in the tension and compression samples are caused by the intersections of multiple variants. When there are many intersections, the twins are more plate-shaped and are bounded by two large, parallel, ($0\bar{1}12$) planes. When there are fewer intersections, the twins are wedge-shaped and are bounded by the ($0\bar{1}11$) with ($01\bar{1}3$) planes.

Declaration of competing interest

The authors declare that they have no known competing financial interests or personal relationships that could have appeared to influence the work reported in this paper.

Acknowledgements

The authors thank Dr. William Lenthe and Xiaoting Zhong for assistance with elements of the data processing and Dr. Cyril Williams for providing the deformed samples. This work was supported by a grant from the Army Research Laboratory through Cooperative Agreement W911NF-12-2-0065. G.S.R. acknowledges additional support from the National Science Foundation (DMREF-1628994). The authors acknowledge the use of the Materials Characterization Facility at Carnegie Mellon University supported by grant MCF-677785.

References

[1] E.W. Kelley, W.F. Hosford, Plane-strain compression of magnesium and magnesium alloy crystals, Trans. Metall. Soc. AIME 242 (1968) 5–13.
[2] E.W. Kelley, W.F. Hosford, Deformation characteristics of textured magnesium, Trans. Metall. Soc. AIME 242 (1968) 654–661.
[3] M.R. Barnett, Twinning and the ductility of magnesium alloys part I: "tension" twins, Mater Sci Eng A Struct Mater 464 (2007) 1–7, https://doi.org/10.1016/j.msea.2006.12.037.
[4] M.R. Barnett, Twinning and the ductility of magnesium alloys Part II. "contraction" twins, Mater Sci Eng A Struct Mater 464 (2007) 8–16, https://doi.org/10.1016/j.msea.2007.02.109.
[5] D. Ando, J. Koike, Y. Sutou, Relationship between deformation twinning and surface step formation in AZ31 magnesium alloys, Acta Mater. 58 (2010) 4316–4324 https://doi.org/10.1016/j.actamat.2010.03.044.
[6] S.-G. Hong, S.H. Park, C.S. Lee, Role of {10-12} twinning characteristics in the deformation behavior of a polycrystalline magnesium alloy, Acta Mater. 58 (2010) 5873–5885 https://doi.org/10.1016/j.actamat.2010.07.002.
[7] M. Lentz, M. Risse, N. Schaefer, W. Reimers, I.J. Beyerlein, Strength and ductility with {10-11} - {10-12} double twinning in a magnesium alloy, Nat. Commun. 7 (2016), https://doi.org/10.1038/ncomms11068.
[8] C. Guo, R. Xin, Y. Xiao, G. Liu, Q. Liu, Observation and analysis of the coexistence of two "opposite" twin modes in a Mg-Al-Zn alloy, Mater. Des. 102 (2016) 196–201 https://doi.org/10.1016/j.matdes.2016.04.034.
[9] J. Koike, Enhanced deformation mechanisms by anisotropic plasticity in polycrystalline Mg alloys at room temperature, Metall. Mater. Trans. A 36A (2005) 1689–1696, https://doi.org/10.1007/s11661-005-0032-4.
[10] M.D. Nave, M.R. Barnett, Microstructures and textures of pure magnesium deformed in plane-strain compression, Scripta Mater 51 (2004) 881–885 https://doi.org/10.1016/j.scriptamat.2004.07.002.

[11] M.Z. Bian, K.S. Shin, {10-12} twinning behavior in magnesium single crystal, Met. Mater. Int. 19 (2013) 999–1004, https://doi.org/10.1007/s12540-013-5012-4.
[12] I.J. Beyerlein, L. Capolungo, P.E. Marshall, R.J. McCabe, C.N. Tome, Statistical analyses of deformation twinning in magnesium, Phil Mag 90 (2010) 2161–2190 https://doi.org/10.1080/14786431003630835.
[13] Z.Z. Shi, Y.D. Zhang, F. Wagner, T. Richeton, P.A. Juan, J.S. Lecomte, L. Capolungo, S. Berbenni, Sequential double extension twinning in a magnesium alloy: combined statistical and micromechanical analyses, Acta Mater. 96 (2015) 333–343 https://doi.org/10.1016/j.actamat.2015.06.029.
[14] D. Sun, M. Ponga, K. Bhattacharya, M. Ortiz, Proliferation of twinning in hexagonal close-packed metals: application to magnesium, J Mech Phys Solids 112 (2018) 368–384, https://doi.org/10.1016/j.jmps.2017.12.009.
[15] B.A. Bilby, A.G. Crocker, Theory of crystallography of deformation twinning, Proc R Soc Lond A Math Phys Sci 288 (1965) 240–255, https://doi.org/10.1098/rspa.1965.0216.
[16] J.W. Christian, D.E. Laughlin, The deformation twinning of superlattice structures derived from disordered BCC or FCC solid-solutions, Acta Metall. 36 (1988) 1617–1642, https://doi.org/10.1016/0001-6160(88)90230-1.
[17] J.W. Christian, S. Mahajan, Deformation twinning, Prog. Mater. Sci. 39 (1995) 1–157 https://doi.org/10.1016/0079-6425(94)00007-7.
[18] G.S. Rohrer, D.M. Saylor, B. El Dasher, B.L. Adams, A.D. Rollett, P. Wynblatt, The distribution of internal interfaces in polycrystals, Z Metallkd 95 (2004) 197–214.
[19] L. Capolungo, P.E. Marshall, R.J. McCabe, I.J. Beyerlein, C.N. Tome, Nucleation and growth of twins in Zr: a statistical study, Acta Mater. 57 (2009) 6047–6056 https://doi.org/10.1016/j.actamat.2009.08.030.
[20] A. Khosravani, D.T. Fullwood, B.L. Adams, T.M. Rampton, M.P. Miles, R.K. Mishra, Nucleation and propagation of {10-12} twins in AZ31 magnesium alloy, Acta Mater. 100 (2015) 202–214 https://doi.org/10.1016/j.actamat.2015.08.024.
[21] S. Lay, G. Nouet, Morphology of (01-12) twins in zinc and related interfacial defects, Phil Mag A 72 (1995) 603–617 https://doi.org/10.1080/01418619508243788.
[22] X.Y. Zhang, B. Li, X.L. Wu, Y.T. Zhu, Q. Ma, Q. Liu, P.T. Wang, M.F. Horstemeyer, Twin boundaries showing very large deviations from the twinning plane, Scripta Mater 67 (2012) 862–865 https://doi.org/10.1016/j.scriptamat.2012.08.012.
[23] Q. Yu, J. Wang, Y.Y. Jiang, R.J. McCabe, N. Li, C.N. Tome, Twin-twin interactions in magnesium, Acta Mater. 77 (2014) 28–42, https://doi.org/10.1016/j.actamat.2014.05.030.
[24] W. Wu, Y. Gao, N. Li, C.M. Parish, W. Liu, P.K. Liaw, K. An, Intragranular twinning, detwinning, and twinning-like lattice reorientation in magnesium alloys, Acta Mater. 121 (2016) 15–23 https://doi.org/10.1016/j.actamat.2016.08.058.
[25] A. Fernandez, A. Jerusalem, I. Gutierrez-Urrutia, M.T. Perez-Prado, Three-dimensional investigation of grain boundary-twin interactions in a Mg AZ31 alloy by electron backscatter diffraction and continuum modeling, Acta Mater. 61 (2013) 7679–7692 https://doi.org/10.1016/j.actamat.2013.09.005.
[26] H. Abdolvand, M. Majkut, J. Oddershede, S. Schmidt, U. Lienert, B.J. Diak, P.J. Withers, M.R. Daymond, On the deformation twinning of Mg AZ31B: a three-dimensional synchrotron X-ray diffraction experiment and crystal plasticity finite element model, Int J Plasticity 70 (2015) 77–97 https://doi.org/10.1016/j.ijplas.2015.03.001.
[27] M.A. Groeber, B.K. Haley, M.D. Uchic, D.M. Dimiduk, S. Ghosh, 3D reconstruction and characterization of polycrystalline microstructures using a FIB-SEM system, Mater. Charact. 57 (2006) 259–273 https://doi.org/10.1016/j.matchar.2006.01.019.
[28] M.N. Kelly, K. Glowinski, N.T. Nuhfer, G.S. Rohrer, The five parameter grain boundary character distribution of alpha-Ti determined from three-dimensional orientation data, Acta Mater. 111 (2016) 22–30 https://doi.org/10.1016/j.actamat.2016.03.029.
[29] C.S. Kim, A.D. Rollett, G.S. Rohrer, Grain boundary planes: new dimensions in the grain boundary character distribution, Scripta Mater 54 (2006) 1005–1009 https://doi.org/10.1016/j.scriptamat.2005.11.071.
[30] G.S. Rohrer, Grain boundary energy anisotropy: a review, J. Mater. Sci. 46 (2011) 5881–5895 https://doi.org/10.1007/s10853-011-5677-3.
[31] M.A. Groeber, M.A. Jackson, DREAM.3D: a digital representation environment for the analysis of microstructure in 3D, Integrating Materials and Manufacturing Innovation 3 (2014) 5.
[32] K. Glowinski, A. Morawiec, Analysis of experimental grain boundary distributions based on boundary-space metrics, Metall. Mater. Trans. A 45A (2014) 3189–3194, https://doi.org/10.1007/s11661-014-2325-y.
[33] S.J. Dillon, G.S. Rohrer, Characterization of the grain-boundary character and energy distributions of yttria using automated serial sectioning and EBSD in the FIB, J. Am. Ceram. Soc. 92 (2009) 1580–1585 https://doi.org/10.1111/j.1551-2916.2009.03064.x.
[34] J. Li, S.J. Dillon, G.S. Rohrer, Relative grain boundary area and energy distributions in nickel, Acta Mater. 57 (2009) 4304–4311 https://doi.org/10.1016/j.actamat.2009.06.004.
[35] G.S. Rohrer, J. Li, S. Lee, A.D. Rollett, M. Groeber, M.D. Uchic, Deriving grain boundary character distributions and relative grain boundary energies from three-dimensional EBSD data, Mater Sci Tech 26 (2010) 661–669 https://doi.org/10.1179/026708309X12468927349370.
[36] J.T. Lloyd, A dislocation-based model for twin growth within and across grains, Proc. Royal Soc. A 474 (2018), https://doi.org/10.1098/rspa.2017.0709.
[37] B.-Y. Liu, J. Wang, B. Li, L. Lu, X.-Y. Zhang, Z.-W. Shan, J. Li, C.-L. Jia, J. Sun, E. Ma, Twinning-like lattice reorientation without a crystallographic twinning plane, Nat. Commun. 5 (2014), https://doi.org/10.1038/ncomms4297.
[38] A. Ostapovets, J. Bursik, R. Groger, Deformation due to migration of faceted {10-12} twin boundaries in magnesium and cobalt, Phil Mag 95 (2015) 4106–4117, https://doi.org/10.1080/14786435.2015.1115134.
[39] V. Paidar, A. Ostapovets, The balance between the energies of the symmetric (10-12) twin boundaries and asymmetric basal/prismatic interfaces in hcp metals, Mater. Lett. 198 (2017) 93–96 https://doi.org/10.1016/j.matlet.2017.03.178.
[40] V. Paidar, A. Ostapovets, T. Kana, Dislocation content of non-classical twin boundaries in hexagonal metals, Acta Phys. Pol. A 134 (2018) 692–694, https://doi.org/10.12693/APhysPolA.134.692.
[41] A. Ostapovets, A. Serra, Characterization of the matrix-twin interface of a (10-12) twin during growth, Phil Mag 94 (2014) 2827–2839, https://doi.org/10.1080/14786435.2014.933906.
[42] A. Serra, D.J. Bacon, A new model for {10-12} twin growth in hcp metals, Phil Mag A 73 (1996) 333–343 https://doi.org/10.1080/01418619608244386.
[43] A. Serra, D.J. Bacon, R.C. Pond, Dislocations in interfaces in the hcp metals - I. defects formed by absorption of crystal dislocations, Acta Mater. 47 (1999) 1425–1439 https://doi.org/10.1016/s1359-6454(99)00016-6.
[44] H. El Kadiri, C.D. Barrett, J. Wang, C.N. Tome, Why are {10-12} twins profuse in magnesium? Acta Mater. 85 (2015) 354–361, https://doi.org/10.1016/j.actamat.2014.11.033.